Letters in Applied NanoBioScience
Open-Access Journal (ISSN: 2284-6808)

Article
Volume 15, Issue 3, 2026, 91
https://doi.org/10.33263/LIANBS153.091

Computational Evaluation of New 2-Aminothiazole Derivatives as Anti-Inflammatory Agents

Mallikarjunaswamy Pramod [1], Deshavalli Puttarajegowda Prashanth [1], Shanthappa Nanjundaswamy [1,*], Santhosh Arehalli Shivamurthy [2], Sandeep Shadakshari [1], Puttaswamappa Mallu [1]

[1] Department of Chemistry, SJCE, JSS Science and Technology University, Mysuru 570 006, India
[2] Department of Chemistry (U.G.), N.M.K.R.V. College for Women, Bangalore, Karnataka 560011, India
* Correspondence: nswamychem@jssstuniv.in;

Received: 24.01.2025; Accepted: 22.02.2026; Published: 01.07.2026

Abstract: Inflammation is a biological process implicated in numerous chronic diseases, such as rheumatoid arthritis, psoriasis, and inflammatory bowel disease. Dysregulated inflammatory signaling is primarily mediated by Tumor Necrosis Factor-alpha (TNF-α), which is identified as a major contributor to the progression of these conditions. This present work aims to discover a potential anti-inflammatory agent using structural and ligand-based *in silico* approaches. A set of 144 substituted 2-aminothiazole derivatives was designed by substituting the R1 and R2 positions to optimize their anti-inflammatory potential. Using ligand-based pharmacophore modeling followed by 3D-QSAR, 55 active compounds were selected based on predicted IC50 values. Subsequent ADMET analysis confirmed that the drug-likeness properties of 30 compounds were substantial, and they were subjected to molecular docking against the TNF-α protein (PDB ID: 2AZ5) alongside the standard drug meloxicam. Docking frrrrrrrresults exhibited a strong binding score for several derivatives, among them compound-8b (2-((4-hydroxyphenyl)amino)-5-(7-methylbenzo[d][1,3]dioxol-5-yl)-5,6-dihydrobenzo[d]thiazol-7(4H)-one) emerged as the lead candidate with a significant binding score compared to the standard drug. Additionally, molecular dynamics (MD) simulation results for compound-8b demonstrated superior stability and pharmacokinetic profiles compared to the standard drug, highlighting its potential to efficiently block TNF-α-mediated inflammatory pathways and to evaluate its efficacy as an anti-inflammatory agent.

Keywords: inflammation; thiazole derivatives; *in silico*; TNF-α; molecular docking and MD simulation.

1. Introduction

Thiazole, a five-membered heterocyclic compound comprising nitrogen and sulfur atoms, serves as a pivotal scaffold in medicinal chemistry due to its extensive pharmacological profile [1]. It has emerged as a promising candidate in many fields, including research on antifungal, anti-inflammatory, antibacterial, antioxidant, anticonvulsant, antiallergic, herbicidal, anti-HIV, antidiabetic, anticancer, and insecticidal agents [2]. Also, thiazole derivatives are powerful medicines against a variety of malignancies due to their ability to alter multiple biological pathways (receptors) [3,4]. The various modes of action, such as altering gene expression and interfering with cellular signaling networks, also highlight its potential for

therapeutic use [5]. Additionally, new thiazole compounds with enhanced potency and selectivity have been synthesized using advancements in synthetic organic chemistry, paving the way for the development of different types of therapies [6].

Due to numerous environmental factors, aging populations, and changes in lifestyle, the prevalence of diseases associated with inflammation has increased dramatically worldwide [7]. Chronic inflammatory illnesses are thought to be responsible for over 50% of fatalities globally, which highlights their significant influence on public health [8]. Inflammation is a complex and carefully regulated biological process that forms part of the innate immune response, which acts as the body's primary defense against harmful stimuli such as poisons, infections, and damaged cells. It is characterized by redness, swelling, heat, pain, and loss of function, which collectively aim to eliminate the causative agent, clear damaged tissues, and promote healing. This process includes the release of inflammatory mediators, the activation and modulation of immune cells, and the modulation of vascular responses [9]. While acute inflammation is protective and resolves once the threat is neutralized, chronic or dysregulated inflammation can lead to tissue damage and the emergence of various diseases like rheumatoid arthritis, cardiovascular diseases, diabetes, neurodegenerative disorders (e.g., Alzheimer's and Parkinson's), cancer, and autoimmune conditions such as lupus and multiple sclerosis [10]. Among them, inflammation is orchestrated through complex signaling pathways that regulate immune responses and mediate inflammatory processes. Key pathways include NF-κB and MAPK, which stimulate the production of pro-inflammatory cytokines such as TNF-α, IL-1, and IL-6, mainly in response to microbial infection or stress in humans [11]. One of them is Tumor Necrosis Factor-alpha (TNF-α), which plays a crucial part. TNF-α, primarily produced by macrophages and T-cells, binds to two receptors, TNFR1 and TNFR2, initiating distinct signaling pathways. TNFR1, expressed ubiquitously, mediates inflammatory responses, cell survival, and apoptosis by activating the NF-κB and MAPK pathways, which control the production of cytokines that promote inflammation, adhesion molecules, and enzymes such as COX-2. TNFR2, predominantly found on immune and endothelial cells, supports cell proliferation and tissue repair [12,13]. TNF-α promotes inflammation through mechanisms such as vasodilation and edema formation via nitric oxide and prostaglandins, leukocyte adhesion via upregulation of ICAM-1 and VCAM-1, and stress induced by reactive oxygen species (ROS). Additionally, TNF-α links inflammation to coagulation by enhancing tissue factor expression and suppressing fibrinolysis, while acting as a pyrogen to induce fever through prostaglandin synthesis in the hypothalamus [14]. Dysregulated TNF-α signaling contributes to chronic inflammation and underlies rheumatoid arthritis and other conditions, such as inflammatory bowel disease and psoriasis. It is also implicated in inflammation-driven carcinogenesis, promoting angiogenesis, tumor growth, and metastasis [15]. Anti-TNF therapies, such as meloxicam and adalimumab, have revolutionized the treatment of autoimmune and inflammatory diseases by effectively modulating TNF-α activity, highlighting its critical role in pathological inflammation and therapeutic interventions [16]. In contrast, the FDA has approved many synthetic drugs, especially for anti-inflammatory treatments, such as Methotrexate, Tofacitinib, Baricitinib, Apremilast, Leflunomide, Celecoxib, and Meloxicam (Figure 1a), and so on [17].

Our interest is in discovering a novel substituted 2-aminothiazole, which resulted in anti-inflammatory activity and led us to the design of *5-(benzo[1,3]-dioxol-5-yl)-2-(phenylamino)-5,6-dihydrobenzo-thiazol-7(4H)-one* (Figure 1b) derivatives [18]. In this present research, we have designed and created 144 *5-(benzo[1,3]-dioxol-5-yl)-2-*

(phenylamino)-5,6-dihydrobenzo-thiazol-7(4H)-one derivatives to validate them as anti-inflammatory agents, also to evaluate their potential as anti-inflammatory agents, and to discover a lead compound to inhibit pro-inflammatory cytokines TNF-α. The development and design of 2-aminothiazole derivatives aim to enhance biological activity and maintain the molecules' efficacy. Halides, nitro, hydroxyl, methoxy, amino, methyl, and carboxylic acid groups were introduced at the R1 position, and the same substituent systems were substituted at the R2 position, which resulted in a possible way in the formation of 144 pharmacophore models (Table 1) [19]. The hydrophobic character was anticipated to grow as a result of these alterations. Additionally, using 3D QSAR analyses, we identified a potentially effective pharmacophore for the corresponding biological activity. Using computational tools such as ADMET analysis, Molecular docking, and MD simulation, the lead candidate was identified and assessed [20].

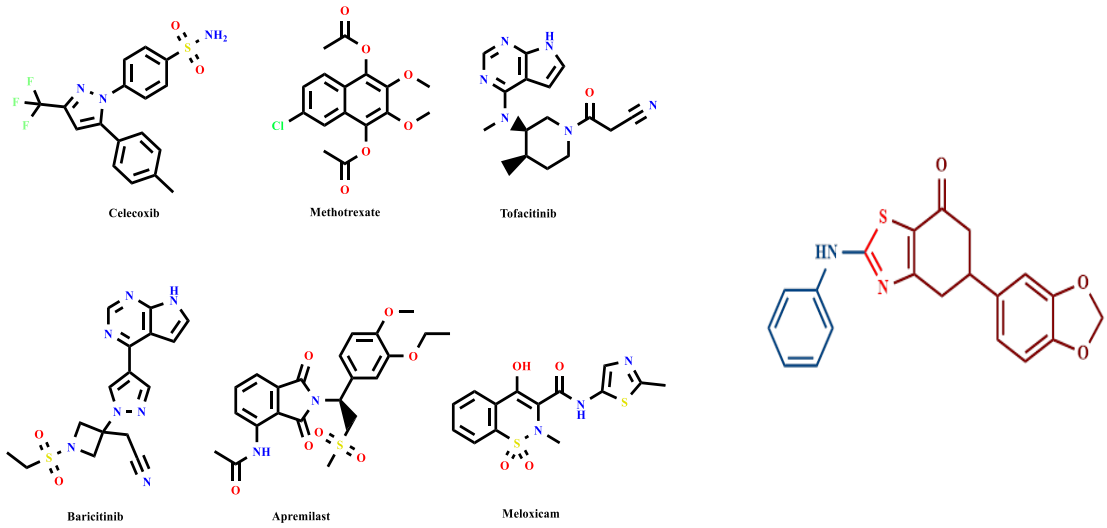

Figure 1. (a) Some of the FDA-approved drugs for inflammatory treatment; **(b)** 5-(benzo[1,3]-dioxol-5-yl)-2-(phenylamino)-5,6-dihydrobenzo-thiazol-7(4H)-one.

2. Materials and Methods

2.1. Network analysis and pass online target prediction.

The biological activity of 2-aminothiazole derivatives was forecasted using the Prediction of Activity Spectra for Substances (PASS) online tool (http://www.way2drug.com/PASSOnline/). The 2-aminothiazole derivatives were submitted in the form of canonical SMILES, and the probability of activity (Pa) and inactivity (Pi) for each compound across different biological targets was calculated. The obtained result showed that the highest probability of activity (Pi) is for the Anaphylatoxin receptor antagonist, with a score of 0.812, which is related to inflammatory conditions and immune system dysregulation [21].

2.2. Obtaining the target for the 2-aminothiazole compound and inflammation.

To identify potential target proteins for the compound (i.e., 2-aminothiazole), we used several target prediction databases, including Swiss target prediction, SuperPred (http://prediction.charite.de/), and Targetnet (http://targetnet.scbdd.com/) [22]. These databases facilitate the prediction of proteins that are associated with the compound, in the form of UniProt IDs. Then, for the disease target prediction (i.e., inflammation-related

proteins), we utilized two comprehensive databases: Genecards (https://www.genecards.org/) [23] and Uniprot (https://www.uniprot.org/). These databases helped in the collection of inflammation-related proteins in the form of UniProt IDs [24,25]. To refine our analysis, we identified overlapping proteins that were both targeted by the 2-aminothiazole compound and associated with inflammation. This was achieved by employing Venny 2.1 (https://bioinfogp.cnb.csic.es/tools/venny/) [26], a web-based tool for generating Venn diagrams, which helps to extract the common proteins from both the data sets.

2.3. Construction of PPI network and Identification of hub proteins.

The most common proteins were identified using Venny 2.1, which were both targeted by the 2-aminothiazole compound and associated with inflammation, and were imported into Cytoscape (version 3.10.2), where the STRING database plugin was used to construct the PPI Network [27]. The resulting PPI network was visualized and analyzed. The core targets within the PPI network were identified using the CytoHubba plugin, and the top 10 targets were independently selected based on the 4 scoring methods: MNC, MCC, Degree, and Closeness [28]. The intersection of these 4 scores was selected for further refinement and analysis.

2.4. KEGG pathway analysis.

To begin with, the top 10 intersecting proteins identified employing Cytohubba were converted into Entrez IDs to eliminate errors caused by capitalization or abbreviations in target names. Then the resulting Entrez IDs were examined using the DAVID tool (DAVID Functional Annotation Tools) [29]. Subsequently, KEGG pathway analysis was performed to assess the involvement of the top 10 proteins in pathways related to inflammation. Furthermore, the proteins involved in inflammation were examined to elucidate their specific roles within the inflammatory pathways, thereby clarifying their potential impact on inflammation and their relevance as therapeutic targets.

2.5. Pharmacophore and 3D-QSAR (3D-quantitative structure-activity relationships) study.

When the macromolecular target structure is unavailable, a ligand-based pharmacophore model serves as a vital computational tool for advancing drug discovery. Various techniques, such as energy- or geometry-based methods, can be used to analyze proteins to identify potential compounds that interact with active sites. Following identification, these active sites were transformed into pharmacophore features [30]. Structure-based pharmacophore modeling involves incorporating selected features into a pharmacophore model by evaluating the chemical properties of the active site and their spatial relationships [31].

Pharmacophore modeling was carried out employing Schrödinger's phase 3.0 module, an important drug design suite [32]. This phase provided 6 inherent pharmacophore features: hydrogen bond donor (D), hydrogen bond acceptor(A), hydrophobic group (H), negatively ionizable (N), positively ionizable (p), and an aromatic ring (R). Compounds were minimized utilizing an optimal method that converged on the gradient to refine their conformation. Subsequently, flexible compound alignment was applied, which resulted in combinations that demonstrated optimal alignment and compatibility with each active compound [33]. These compounds were then screened against four different model features during the validation phase and filtered based on their fitness scores and compound alignment. The highest-scoring

pharmacophore hypothesis, designated ADHRR_1, was selected as the basis for a 3D-QSAR model via substituent modification. In contrast to pharmacophore models, the QSAR model considers the entire molecular structure of the compound to precisely analyze the correlation between the compound's structure and activity, known as the structure-activity relationship (SAR). This relationship is demonstrated in a conventional QSAR model by representing the compound with van der Waals spheres. Ultimately, a grid interval of 1Å and four PLS factors, which were generated, were utilized to create the QSAR model [34].

2.6. ADMET studies.

The compounds' pharmacokinetic and drug-likeness characteristics were evaluated using two standard computational web-based platforms, pkCSM and SwissADME, to obtain parameters for the Absorption, Distribution, Metabolism, Excretion, and Toxicity (ADMET) [35]. These platforms are essential and time-efficient tools in the drug research and development process, including major parameters in the synthesized compounds, such as toxicity prediction, and also provide insights into drug-likeness parameters, such as the Boiled-Egg model and the Bioavailability Radar, which offer visual and graphical representations of the compound's pharmacokinetic profiles. Also, the five rules of drug-likeness properties, such as Lipinski, Ghose, Veber, Egan, and Muegge, were analyzed for all the compounds. The SMILES (Simplified Molecular Input Line Entry System) strings were created after the chemical structures of the compounds were first sketched using ChemDraw Professional 16.0. The generated SMILES notations were subsequently entered into the pkCSM and SwissADME web tools to obtain pharmacokinetic properties [36].

2.7. Molecular docking studies.

2.7.1. Ligand preparation.

Molecular docking studies were performed by employing Auto-dock vina and MGL tools version 1.5.6 to figure out the Binding energy and favorable binding positions of the protein ligand complex. The compound's structures were initially created with ChemDraw Professional 16.0 software, and these chemical structures were modified into 3D models utilizing the Chem 3D 16.0 software tool, which were then saved in PDB format. Auto-Dock tools version 4.2.6 was used to optimize ligand conformations, which were subsequently converted from PDB to PDBQT format for further analysis.

2.7.2. Protein preparation.

The Protein Data Bank (www.rcsb.org) provided the PDB file with respect to the crystal structure of TNF-α (PDB ID: *2AZ5*) [37], a homo-tetramer generated from Homo sapiens. The Biovia Discovery Studio 2019 visualizer was then used to carefully remove solvent molecules and other compounds bound to the protein to generate this protein. Subsequently, nonpolar hydrogen atoms were added to the protein with the help of the AutoDock tool. Finally, the protein's structure was saved in PDBQT format, the preferred input file format for the AutoDock vina application during docking [38,39].

2.7.3. Grid Box generation and virtual screening.

The prepared protein and ligand were docked into the protein's active site employing auto dock vina to assess binding energy, with results reported in kcal/mol [40]. A grid box was constructed to enclose the active site with dimensions of (x=40, y=40, z=40), and its center was positioned at (x=-13.87, y=71.43, z=26.90) to cover the protein's active site accurately. Virtual molecular docking and subsequent analyses were done by using Autodock Vina 1.5.6 version. Each ligand was docked into the defined active site, and the interactions between the protein and ligand were analyzed using the Biovia Discovery Studio 2019 visualizer [41]. Compounds exhibiting good binding score, indicated by the most negative binding energy values, show the most efficient interactions, which were determined, isolated, and chosen for further investigation.

2.8. MD (molecular dynamics) simulation.

Molecular dynamic simulation was carried out at 100 ns intervals using the Schrödinger Desmond 2020-2 package to assess the stability, dynamic behavior, and binding free energy of the protein-ligand complex. The system was prepared using a cubic box containing TIP3P water molecules modeled by the OPLS3 force field. To ensure the system's neutrality, Na^+ ions and salt atoms were introduced. Then the compound undergoes energy minimization through a threshold of kcal/mol Å and proceeds through a 2ns equilibrium phase under the NPT ensemble. This was followed by 20 ns of MD simulation, carried out with a Nose-Hoover thermostat set to 300K and a Marilyn-Tobias barostat operating at 1 bar pressure [42]. The results of MD simulation, including Root mean square deviation (RMSD), Root mean square fluctuation (RMSF), energy potential, and protein-ligand interactions. Considering all these results, we evaluated the complex's stability and flexibility [43].

2.9. MM-GBSA (molecular mechanics-generalized born surface area).

The binding free energy (ΔG) of the protein-ligand complex was estimated using the MM-GBSA technique. MM-GBSA is widely used for its higher accuracy compared to other scoring functions, as it leverages MD simulation analysis of the protein-ligand complex to capture the dynamic nature of molecular interactions within the complex. This approach allows determination of both the energy of the protein-ligand binding complex and that of an isolated compound. The binding free energy calculations were carried out employing the Desmond package's Prime MM-GBSA module, part of the Schrödinger 2020-2 suite. The MM-GBSA methodology was applied in the MD simulation trajectory, which provided a detailed and accurate assessment of the energetic contributions governing the receptor-compound binding stability [44].

3. Results and Discussion

3.1. Network analysis.

In the first phase of the network analysis, Way2Drug's PASS online web-based tool was employed to predict the biological activities of 2-aminothiazole derivatives. This analysis helped in the identification of the unknown protein, which is associated with inflammation. To identify potential receptors inhibited by the selected ligand and linked to inflammation, comprehensive database searches were conducted, revealing 2,410 inflammation-related

proteins and 716 proteins that could be targeted by the 2-aminothiazole derivatives. Employing Venny software, 285 overlapping proteins were identified as both targets of the 2-aminothiazole compound and associated with inflammation (Figure 2). These overlapping proteins were subsequently imported into the Cytoscape software tool for Protein-Protein Interaction (PPI) network analysis (Figure 3). The constructed PPI network comprised 284 nodes, 5440 edges, and an average of 38.310 neighbors, providing a comprehensive overview of interactions among the identified proteins [45].

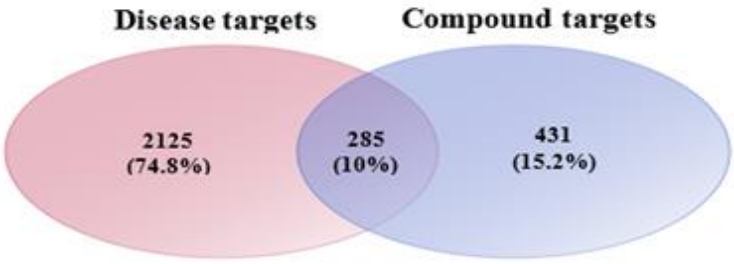

Figure 2. Venny representation of overlapping proteins of the 2-aminothiazole, which are associated with inflammation.

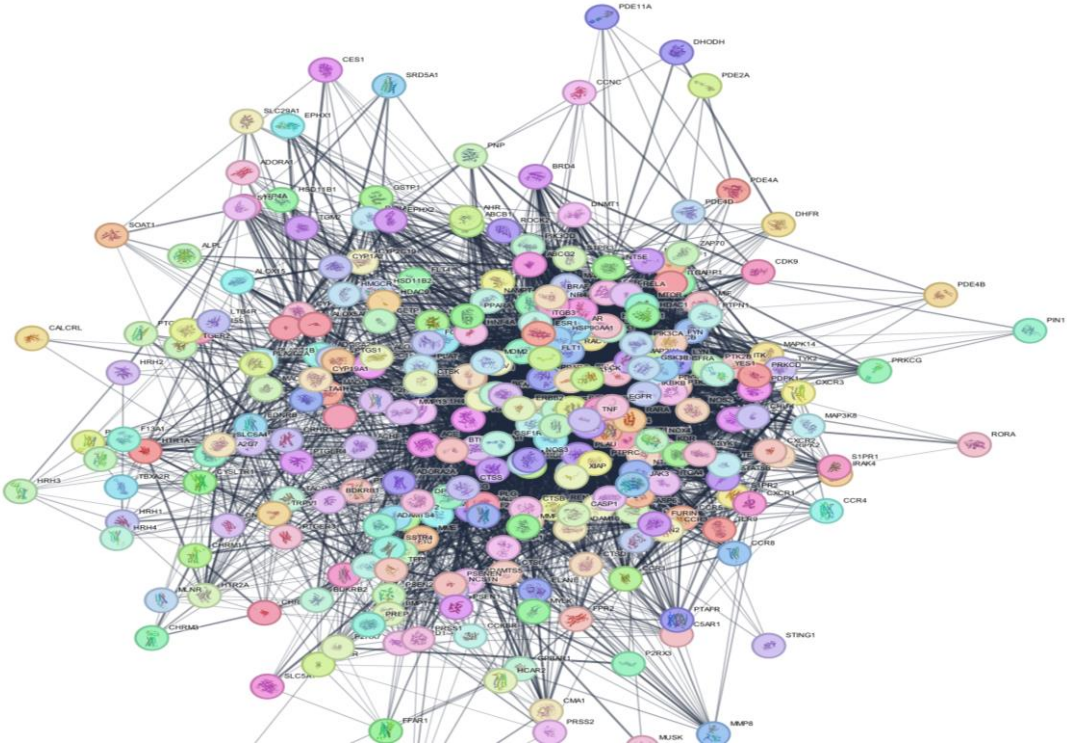

Figure 3. Protein-protein interaction networks of 285 overlapped proteins.

To identify the core components of the PPI network, the CytoHubba plugin in Cytoscape was employed, applying four independent scoring methods: Maximum Neighborhood Component (MNC), Maximal Clique Centrality (MCC), Degree, and Closeness. From this analysis, the top 10 proteins were identified based on their centrality and importance within the network (Figure 4). The intersection of the top 10 proteins derived from the four scoring methods was then subjected to KEGG pathway analysis to identify their involvement in critical biological pathways. Following the identification of 10 proteins through Cytoscape analysis and their subsequent evaluation via KEGG pathway analysis, five proteins, AKT1, PTGS2, TNF, MMP9, and BCL2, were found to be significantly involved in three key

inflammatory pathways: the TNF signaling pathway, IL-17 signaling pathway, and NF-κB signaling pathway (Figure 5).

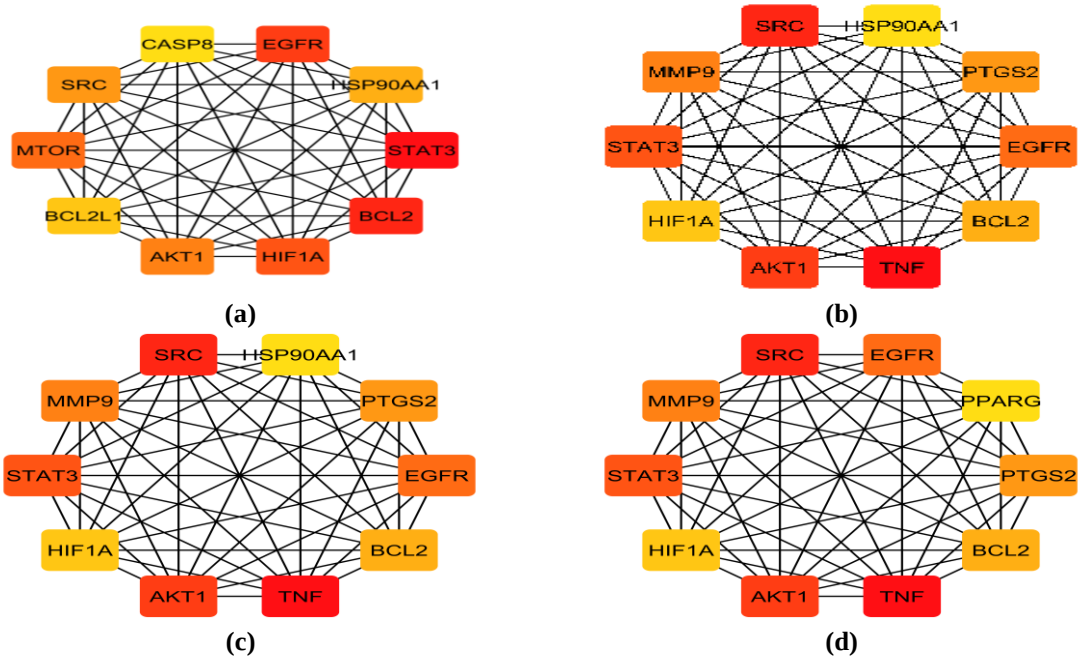

Figure 4. PPI interaction visuals of proteins screened by four algorithms **(a)** MCC; **(b)** MNC; **(c)** Degree; **(d)** Closeness.

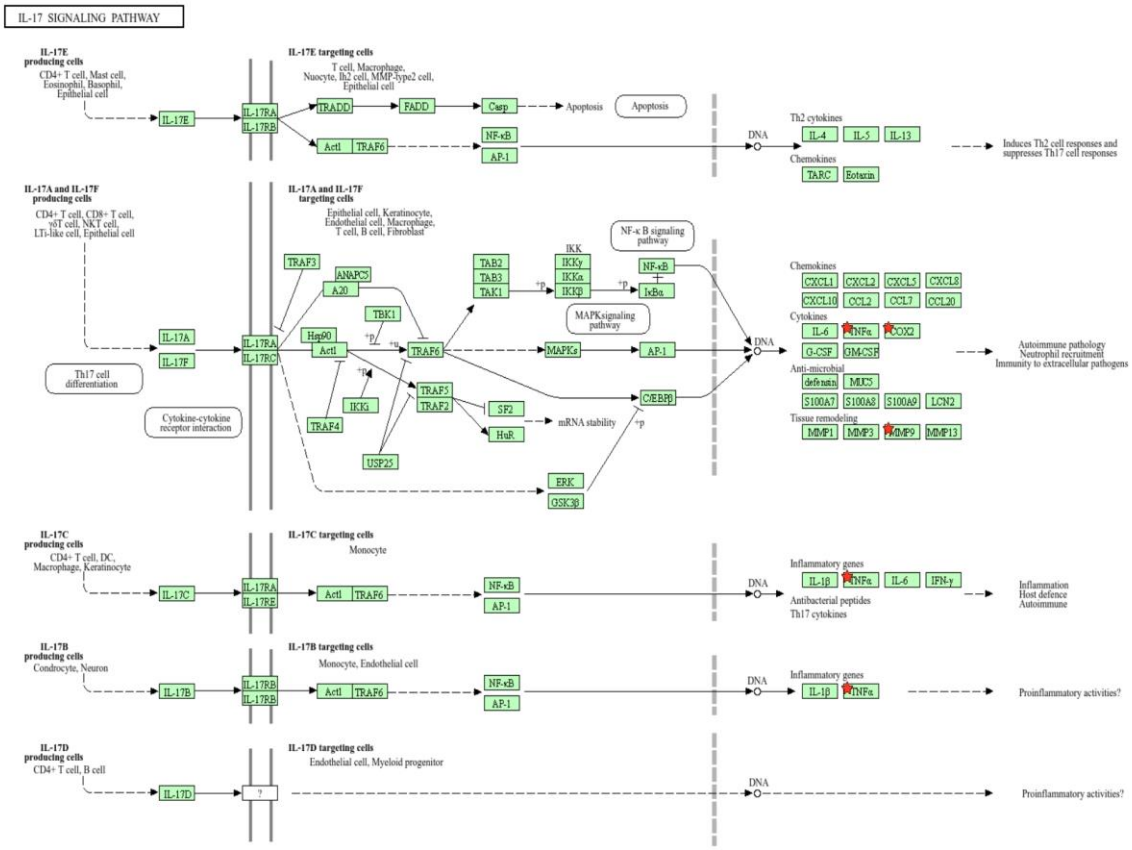

(a)

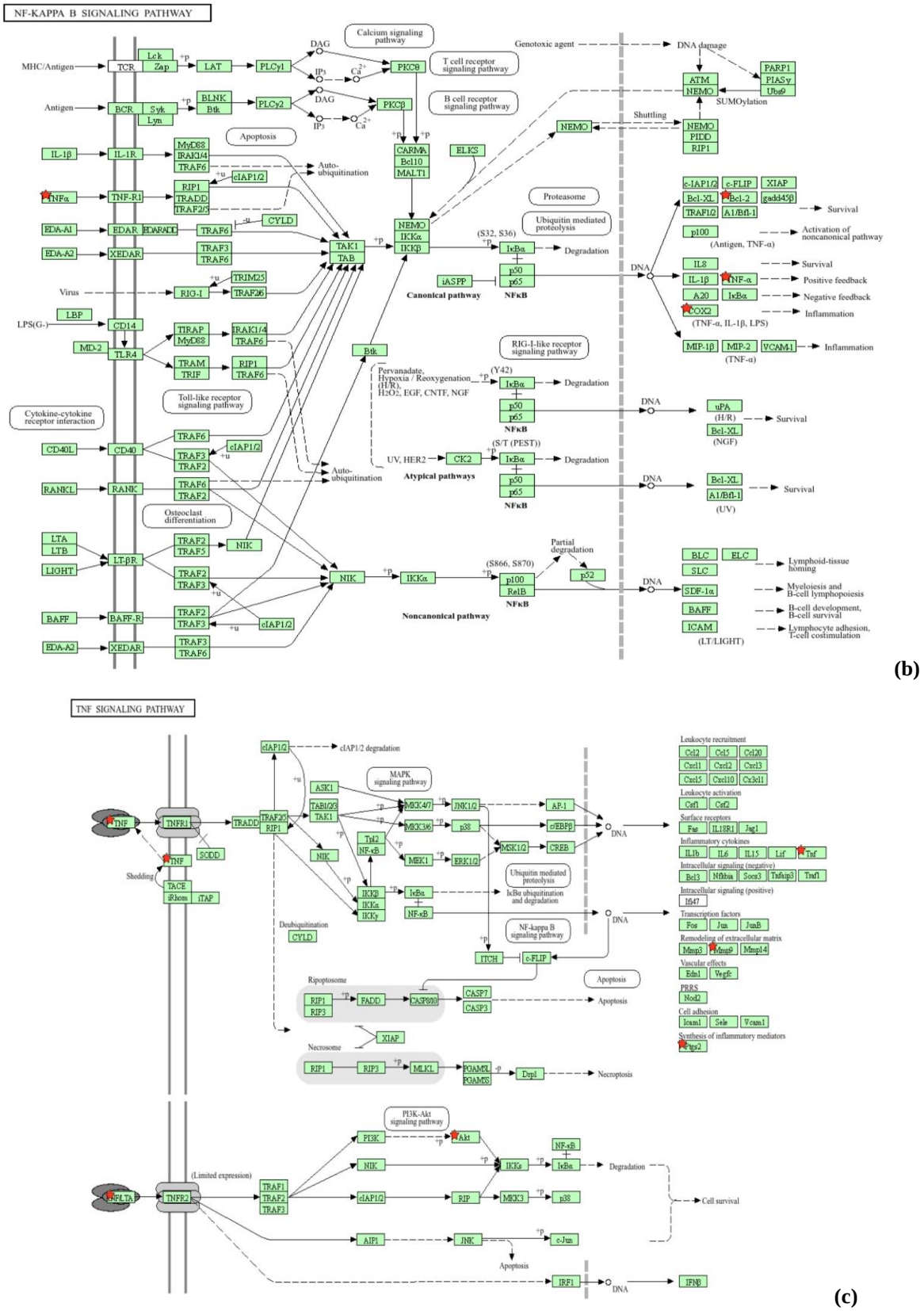

Figure 5. KEGG enrichment diagram of Inflammatory Pathways pathway **(a)** IL-17 signaling pathway; **(b)** NF-κB signaling pathway; **(c)** TNF signaling pathway.

A detailed literature review of these proteins' roles in inflammation identified Tumor Necrosis Factor-alpha (TNF-α) as the most promising therapeutic target. TNF-α plays a central role in regulating inflammatory responses by modulating critical signaling pathways, such as NF-κB and MAPK [46], and activating downstream effectors, including protein kinase B

(AKT1) and cyclooxygenase-2 (COX-2, PTGS2), both of which are pivotal in driving inflammation [47]. TNF-α is an excellent therapeutic target because of its upstream position in the inflammatory pathway; inhibiting it can simultaneously block multiple downstream pathways, offering broad-spectrum control over inflammation. Likewise, chronic inflammatory diseases such as Crohn's disease, psoriasis, and rheumatoid arthritis are directly linked to TNF-α, underscoring its clinical relevance and validation as a therapeutic target [48,49]. In comparison, other highlighted proteins, such as AKT1, PTGS2, MMP9, and BCL2, mainly played downstream or supporting roles in inflammatory pathways [50]. These findings highlight TNF-α as the most promising target for therapeutic strategies against inflammation, compared with other pathway-associated proteins.

3.2. Pharmacophore modeling and 3D-QSAR.

In this research work, pharmacophore modeling was performed using the standard FDA-approved drug meloxicam, along with 144 sets of 2-aminothiazole compounds that have the same core molecule with different substituents, along with structural optimization focused on modifying two distinct regions R1 and R2 of the core pharmacophore Figure 6, resulting in the generation of 144 pharmacophore models. Among them, ADHRR_1 was found to be the most promising one with a maximum survival score of 6.798. To further assess the pharmacophore modeling, we evaluate and record all compounds' fitness, survival, volume, and vector scores, which are mentioned in Table S1. The ADHRR_1 pharmacophore hypothesis, along with pharmacophore modeling results used to guide ligand design in this study, is shown in Figure 7. Figure 7a shows meloxicam, the standard drug, highlighting key features such as hydrogen bond acceptors, donors, and hydrophobic groups essential for TNF-α inhibition. Based on these features, a pharmacophore hypothesis was developed (Figure 7b) that captures the critical interaction points required for biological activity. Figure 7c shows active 2-aminothiazole derivatives that align with the hypothesis, with good preservation of essential features. This suggests that the designed compounds mimic meloxicam's binding characteristics, supporting their potential efficacy as TNF-α inhibitors.

The 3D-QSAR analysis was initiated by selecting all 95 active molecules from the ADHRR_1 pharmacophore hypothesis. Based on this hypothesis, a 3D-QSAR model based on atoms was created. The experimental data set for Anti-inflammatory drugs was randomly partitioned by the software's 70 percent split method based on 4 PLS factors into a 67-compound training set and a 28-compound test set (Table S2). According to the statistical data in Table 2, PLS factor 4 is the best model configuration, as it performs better than the other 3 and shows a stronger fit between predicted and observed biological activities, with an R^2 value of 0.8811. Similarly, the model is very important, as shown by the F-statistic of 114.9 at factor 4, and the RMSE value of 0.01 suggests that the predictions of the models are consistent.

Leave-one-out (LOO) cross-validation on the training set yielded a prediction correlation coefficient (Q2) of 0.66 for anti-inflammatory activity, the highest among the four factors, indicating strong predictive power and stability of the model trained on ADHRR_1. Moreover, a low standard deviation (SD) of 0.006 indicates that the data is suitable for future exploration [51]. As shown in Table 2, a higher F value of 114.9 and a lower P value of 6.06 × 10^-28 emphasize the model's stability and significance, supporting the ADHRR_1 pharmacophore hypothesis. Additionally, Figure 8 presents a linear graph comparing the real activity versus the projected activity of both the training and test sets (Figure 8a), the training

set (Figure 8b), and the test set (Figure 8c), providing a clear visualization of the model's predictive accuracy.

Table 1. Modified substituents for the compound.

Compound. No	Substituent Type (R_1)	Compound group and substituent type (R_2)	Compound. No	Substituent Type (R_1)	Compound group and substituent type (R_2)
1	-H (Hydrogen)	a (-H)	7	$-NO_2$ (Nitro)	g ($-NO_2$)
2	$-CH_3$ (Methyl)	b ($-CH_3$)	8	-OH (Hydroxy)	h (-OH)
3	-Cl (Chloro)	c (-Cl)	9	$-OCH_3$ (Methoxy)	i ($-OCH_3$)
4	-Br (Bromo)	d (-Br)	10	$-NH_2$ (Amino)	j ($-NH_2$)
5	-I (Iodo)	e (-I)	11	$-OC_2H_5$ (Ethoxy)	k ($-OC_2H_5$)
6	-F (Fluro)	f (-F)	12	-COOH (Carboxy)	l (-COOH)

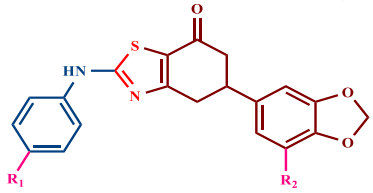

Figure 6 General structure of 5-(benzo[1,3]-dioxol-5-yl)-2-(phenylamino)-5,6-dihydrobenzo-thiazol-7(4H)-one, highlighting variable terminal positions for structure-activity relationship (SAR) optimizations, where R1 and R2 represent aromatic ring-substitutions.

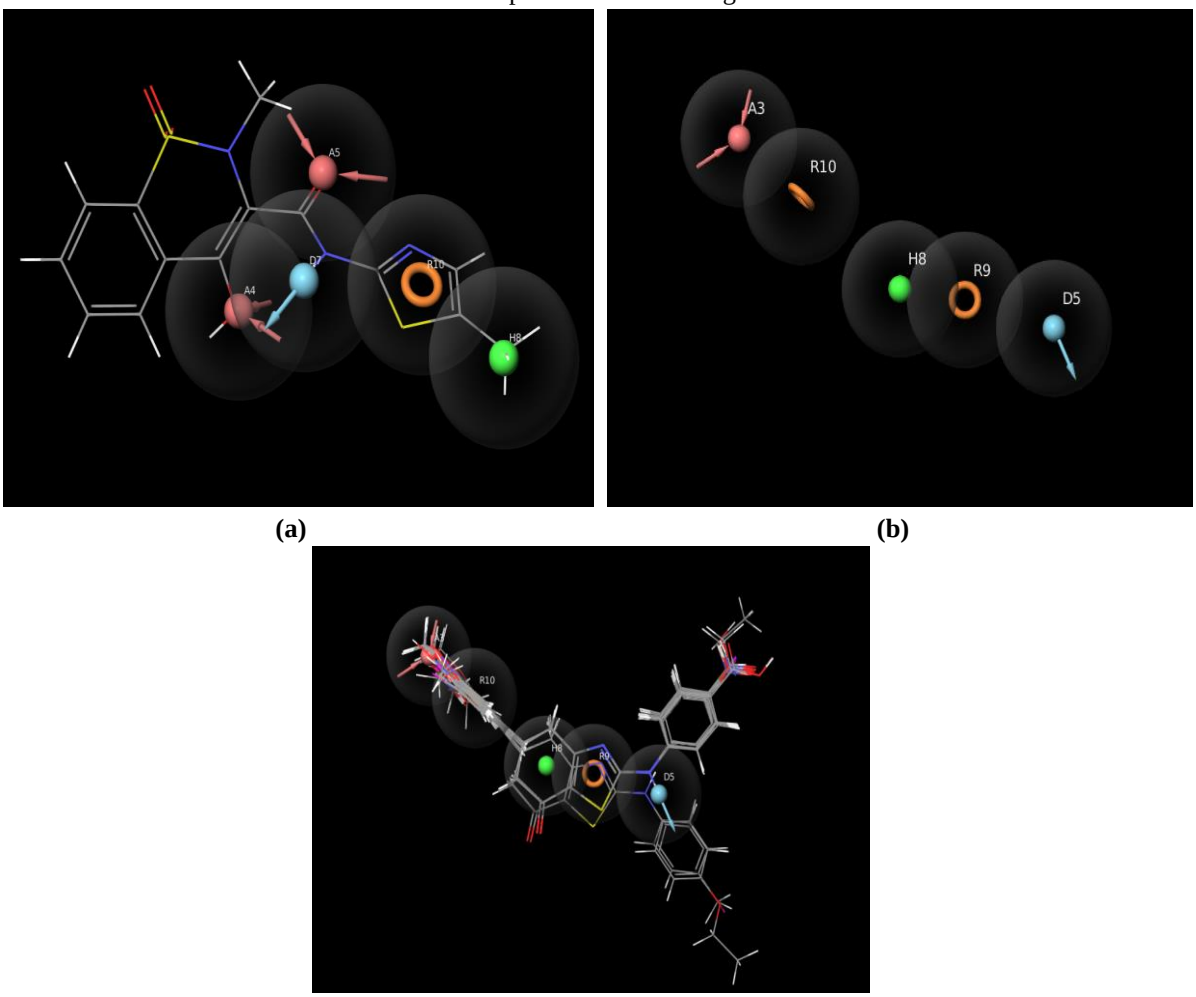

(a) **(b)**

(c)

Figure 7. Pharmacophore model **(a)** Standard drug (Meloxicam); **(b)** Hypothesis developed from standard drug; **(c)** Active ligands overlapped with hypothesis.

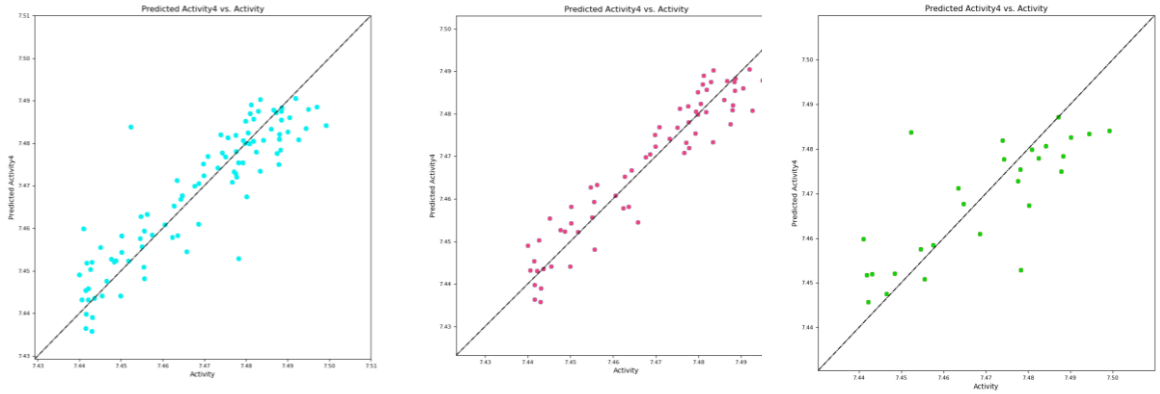

(a) **(b)** **(c)**

Figure 8. Regression plot for predicted activity values for **(a)** Both training and test set; **(b)** Training set; **(c)** Test set.

Table 2. Statistical values of the generated 3D-QSAR model of active compounds.

PLS Factors	SD	R^2	R^2CV	R^2 Scramble	Stability	F	P	RMSE	Q^2	Person-r
1	0.0117	0.5532	0.4491	0.1570	0.978	80.5	5.56e-13	0.01	0.3017	0.5674
2	0.0098	0.6922	0.5658	0.2229	0.974	72	4.19e-17	0.01	0.4487	0.6894
3	0.0071	0.8428	0.7292	0.2500	0.968	112.6	2.9e-25	0.01	0.5566	0.7640
4	0.0062	0.8811	0.7967	0.2650	0.979	114.9	6.06e-28	0.01	0.6671	0.8197

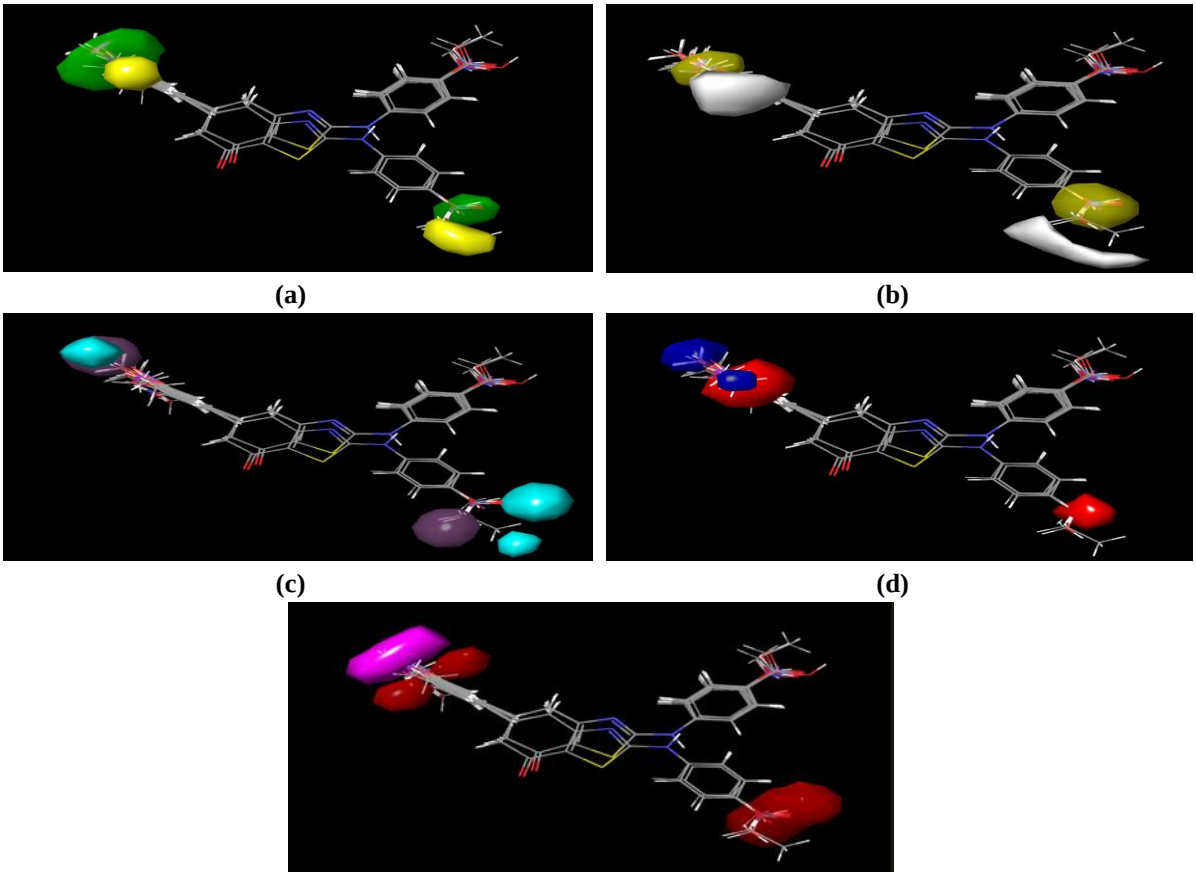

(a) **(b)**

(c) **(d)**

(e)

Figure 9. Representation of ligand-based 3D QSAR **(a)** Gaussian-Steric; **(b)** Gaussian-Hydrophobic; **(c)** Gaussian-H-bond donor; **(d)** Gaussian-Electrostatic; **(e)** Gaussian-H-bond acceptor.

The 3D-QSAR analysis offers valuable insights into the relationship between molecular structure and biological activity, serving as a robust framework for future research [52]. The visual representation of the constructed 3D-QSAR model is illustrated in Figure 9, five distinct

Gaussian field contour maps, Steric (Figure 9a), Hydrophobic (Figure 9b), H-bond donor (Figure 9c), Electrostatic (Figure 9d), and H-bond acceptor (Figure 9e), identify the critical structural features driving target interaction. The statistical validation metrics and predictive parameters derived from these 3D-QSAR fields are summarized in Table 1.

3.3. ADMET analysis.

ADMET and drug-likeness analyses were performed for 55 lead compounds with pIC50 values greater than 7.46, obtained from 3D QSAR data, to determine whether the compounds comply with the 5 drug-likeness properties (Lipinski, Ghose, Veber, Egan, and Muegge) and their pharmacokinetic properties. These criterions concludes whether the compound can administer orally, which includes; i) Lipinski [Molecular weight is ≤ 500 Da,(Approximately 1g/mol), Partition coefficient (log P) ≤ 5, maximum number of hydrogen bond donors-5, maximum number of hydrogen bond acceptors-10, ii) Ghose [Molecular weight between 160–480 Da, Log P (octanol-water partition coefficient) ranging from -0.4 to 5.6, The total number of atoms ranging from 20-70], iii) Veber [rotatable bonds ≤ 10, polar surface area (PSA) ≤ 140 $Å^2$], iv) Egan [log P ≤ 5.88 and polar surface ≤ 131 $Å^2$ (used to predict compound's absorption and permeability)], and v) Muegge[Partition coefficient (log P) ≤ 5, maximum number of hydrogen bond donors-5, number of nitrogen and oxygen atoms between 1 and 9]. Swiss ADME, which was employed to evaluate these 5 rules, is shown in Table S3 in the supplementary information. These rules were accompanied by some of the compounds; others violated the rules, and the compounds with more than 2 violations were eliminated, leaving the remaining compounds.

The pkCSM web application was used to evaluate the toxicological and pharmacokinetic characteristics of 55 selected compounds from 3D QSAR data, which were examined for their ADMET (Absorption, Distribution, Metabolism, Excretion, and Toxicity) parameters, as shown in Table S4 in the supplementary information. Among these 55 compounds, 2a, 1f, 1e, 1j, 1a, 2d, 6f, 2h, 2b, 6j, 6a, 1c, 1d, 5a, 1h, 1b, 6c, 3f, 6h, 6c, 8f, 4a, 8j, 8a, 8c, 8h, 3b, 4b, 8d, and 8b were chosen on the basis of their important intestinal absorption rates such as high water solubility(>90%), and ideal Caco-2 permeability (log Papp >1.3), which signified their effective absorption and decreased outflow potential, these compounds demonstrated lower skin permeability and a positive interaction with P-glycoprotein. Distribution parameter, which indicates their fraction unbound (Fu) and volume of distribution (VDss) values; indicated appropriate distribution properties (log VDss > -0.253). This also showed possible blood-brain barrier (BBB) permeability (> 0.027) for the compounds to act on the central nervous system (CNS). Furthermore, these compounds' metabolic profiles demonstrated interactions with key CYP enzymes (2D6, 3A4, 1A2, 2C19, 2C9) without exhibiting significant inhibitory activity, ensuring their compatibility with metabolic pathways. Additionally, the toxicity profiles, including AMES testing, hERG inhibition experiments, and hepatotoxicity predictions, demonstrated that these compounds had low renal OCT2 substrate activity. Excretion parameter exhibited appropriate overall clearance rates and non-toxic profiles. Furthermore, their safety was confirmed by oral acute and chronic toxicity parameters, which showed encouraging LD_{50} values and chronic exposure tolerance. Considering all of these findings, 30 compounds were selected as good candidates and demonstrated better ADMET characteristics, as shown in the supplementary paper (Table S3), and their positive parameters were supported by thorough pharmacokinetic and toxicological analyses. Likewise, drug-likeness requirements described by the 5 frameworks, Lipinski, Ghose, Veber, Egan, and

Muegge rules, which are demonstrated in Table S4, were also examined to choose these compounds, in which the compounds with few or no violations were given priority and chosen for further molecular docking investigations to obtain an ultimate lead compound. While *in silico* ADMET predictions offer valuable preliminary insights, they require experimental validation due to inherent predictive limitations.

3.4. Molecular docking studies.

Molecular docking studies were conducted to identify a potential lead candidate for TNF-α inhibition. This was performed to examine the binding scores of a set of 30 drug-like candidates selected from ADMET and Drug-likeness analyses with the TNF-α pathway-associated protein (PDB ID: 2AZ5), as shown in Table 3, along with predicted activity pIC50. The soluble version of TNF-α protein, a homo-tetramer generated from Homo sapiens, was selected for these investigations based on its X-ray crystal structure. The 148 amino acids in each chain of this protein structure, are produced in *Escherichia coli* BL21(DE3). The findings of this research are specific to the selected class of chemicals. The *incorporation of a small-molecule compound into the 2AZ5 structure provided important insights into potential therapeutic mechanisms of TNF-α inhibition, underscoring its relevance to* inflammatory disease research and therapeutic applications. Among these 30 compounds, 8b exhibited substantial binding energy with the TNF-α protein, with a binding score of -9.3 kcal/mol, which was greater than that of the FDA-approved standard inflammation drug meloxicam, with a binding score of --7.6 kcal/mol.

Overall, these results showed that 8b had the highest binding energy, making it a more promising TNF-α inhibitor than the other compounds examined. The interaction between 8b and the standard drug with TNF-α protein was also examined in detail. This resulted in the discovery of many amino acids(residues) that are essential for their interaction with the compounds. The molecular interaction analysis of 8b and the standard drug meloxicam with the target protein (*2AZ5*) highlights notable differences in their binding profiles and potential inhibitory efficacies. This study indicates that 8b has a higher potential to inhibit TNF-α protein (2AZ5) than the standard drug meloxicam. 8b formed hydrogen bonds with SER B:60 and LEU B:120 at distances of 2.41Å and 1.80Å, respectively, and established hydrophobic interactions and π-π stacking with TYR A:59, TYR A:151, and HIS A:15, with interaction lengths of 3.90Å, 4.15Å and 4.23Å respectively. These interactions collectively stabilize compound 8b inside the active site of the protein. Conversely, meloxicam displayed hydrogen bonding with TYR B:151, LEU B:120, and GLY B:121, with bond distances of 2.56Å, 3.52Å, and 2.73Å, respectively. And π-π stacking interactions with TYR B:59 and TYR B:119 at distances of 4.32Å and 3.91Å respectively. Additionally, meloxicam exhibited hydrophobic interactions with LEU B:57, contributing to its stable anchoring within the active site. While both compounds showed complementary hydrogen bonding and hydrophobic interactions, 8b demonstrated superior binding characteristics, suggesting it as a more potent candidate for TNF-α inhibition. In contrast, meloxicam is a dependable reference molecule for additional therapeutic research. The binding mode of ligand-8b and meloxicam within the active site of TNF-α (PDB ID: 2AZ5) are shown in Figures 10 amd 11. The 3D (a) and 2D (b) representations detail the precise spatial placement and specific stabilizing interactions with key amino acid residues. Electronic and structural complementarity are further demonstrated by the interpolated charge (c) and aromatic (d) surface representations. These findings clarify the structural prerequisites for efficient compound-8b binding to TNF-α, as shown in Table 4.

Redocking of the co-crystallized ligand from the TNF-α protein structure (PDB ID: *2AZ5*) using the same protocol employed was done, and the docking score for the co-crystalized ligand with protein was found to be -8.0kcal/mol. Furthermore, the RMSD between the redocked pose and the original crystallographic pose was found to be within the acceptable threshold of ≤2 Å, confirming the validity and precision of our docking methodology. RMSD profile of the co-crystalized ligand is demonstrated in the supplementary paper Figure S1.

Table 3. Lead Compounds selected after ADMET analysis with 3D-QSAR model's predicted activity (pIC50) and their Binding Score.

Compounds	Structures	Predicted activity (pIC_{50}) PLS factor-4	Binding score (kcal/mol)
2a	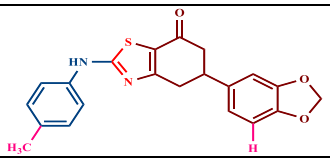	7.46737	-8.8
1f	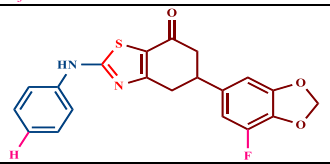	7.46987	-9.3
1e	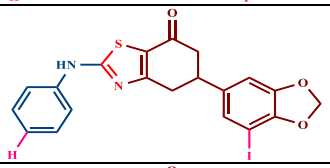	7.47539	-9.1
1j	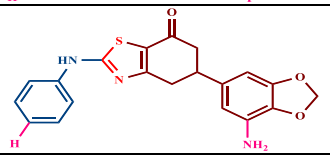	7.47122	-9.0
1a	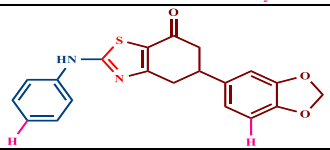	7.47201	-9.1
2d	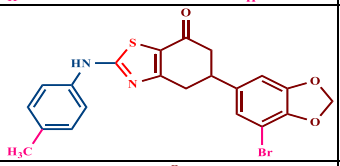	7.47232	-8.5
6f	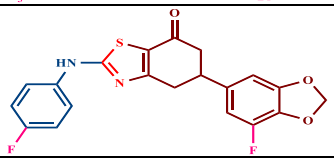	7.47282	-9.0
2h	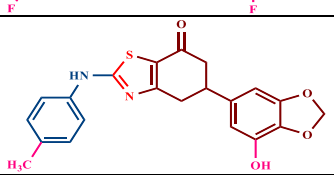	7.47324	-8.6
2b	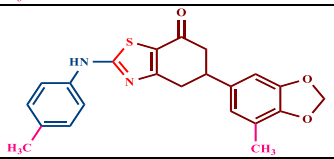	7.4734	-8.7
6j	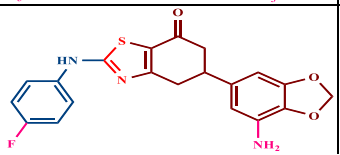	7.47416	-8.7

Compounds	Structures	Predicted activity (pIC_{50}) PLS factor-4	Binding score (kcal/mol)
6a	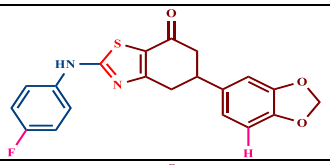	7.47496	-8.9
1c	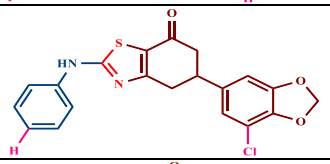	7.47509	-9.3
1d	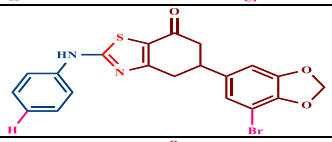	7.47689	-9.2
5a	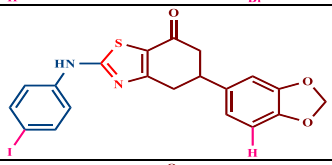	7.47757	-8.7
1h	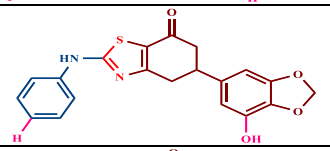	7.47771	-9.0
1b	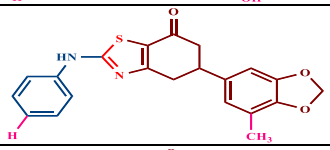	7.4779	-9.0
6c	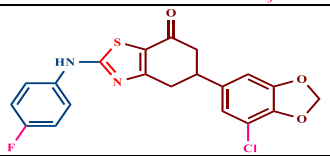	7.47803	-9.0
3f	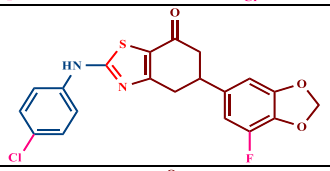	7.47992	-8.6
6h	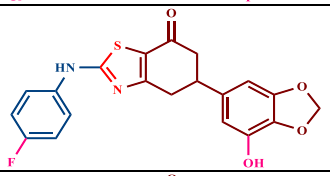	7.48066	-8.6
6b	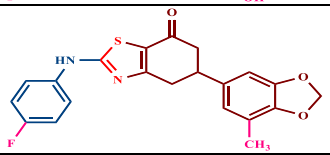	7.48079	-9.3
8f	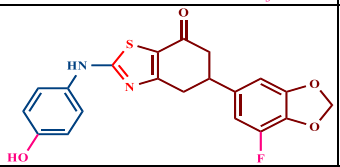	7.48197	-9.3
4a	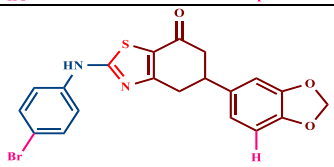	7.48261	-8.7

Compounds	Structures	Predicted activity (pIC_{50}) PLS factor-4	Binding score (kcal/mol)
8j	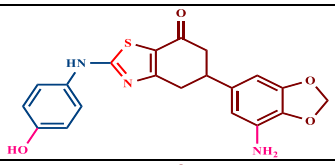	7.48379	-8.5
8a	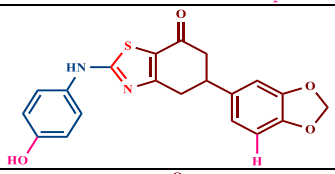	7.48412	-9.2
8c	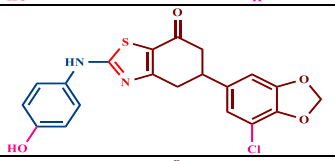	7.48717	-9.2
8h	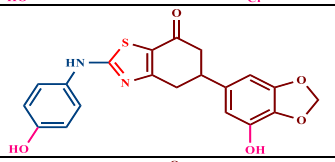	7.49023	-8.9
3b	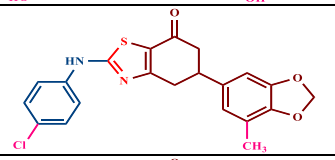	7.48791	-8.6
4b	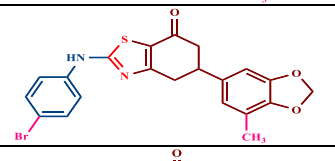	7.48847	-8.6
8d	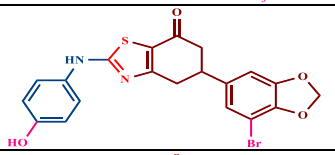	7.48899	-9.1
8b	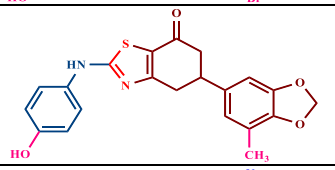	7.49053	-9.3
Standard drug (Meloxicam)	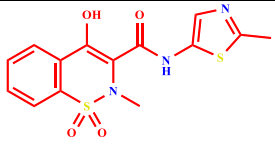	7.5741	-7.6

Table 4. Interaction of compound 8b with the active site residue of TNF-α protein PDB (ID: *2AZ5*).

Protein (PDB ID)	Compound	Protein (amino acids)	Compound Atoms	Interaction type	Distance(Å)	Binding score (kcal/mol)
2AZ5	**8b**	LEU:120	Oxygen	Conventional H-bond	1.80	-9.3
		SER:60			2.41	
		TYR:59	π-Aromatic	π-π-Stacked	3.90	
		TYR:151	Hydrogen	π-Alkyl	4.15	
		HIS:15	Hydrogen	π-Alkyl	4.23	
	Standard drug (Meloxicam)	TYR:151	Oxygen	Conventional H-bond	2.56	-7.6
		LEU:120	Nitrogen	Carbon Hydrogen Bond	2.73	
		GYL:121	Oxygen	Conventional H-bond	3.52	
		TYR:119	π-Aromatic	π-π-Stacked	3.91	
		TYR:59	π-Aromatic	π-π-Stacked	4.32	
		LEU:57	π-Aromatic	Pi-Alkyl	5.40	

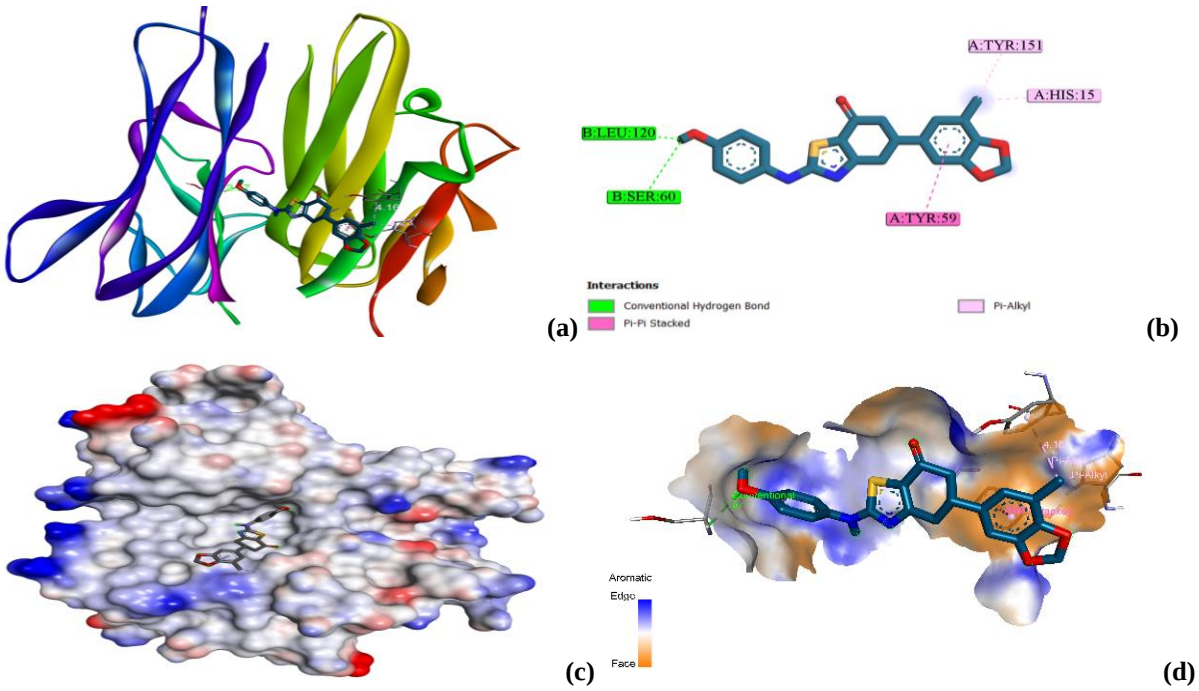

Figure 10. (a) 3D representation of TNF-α Protein(*2AZ5*)-ligand-8b interaction; **(b)** 2D representation of TNF-α protein *2AZ5* (amino acid residues) with ligand-8b interaction; **(c)** Interpolated charge representation of Protein(*2AZ5*)-ligand-8b complex; **(d)** Aromatic representation of Protein(*2AZ5*)-ligand8b complex.

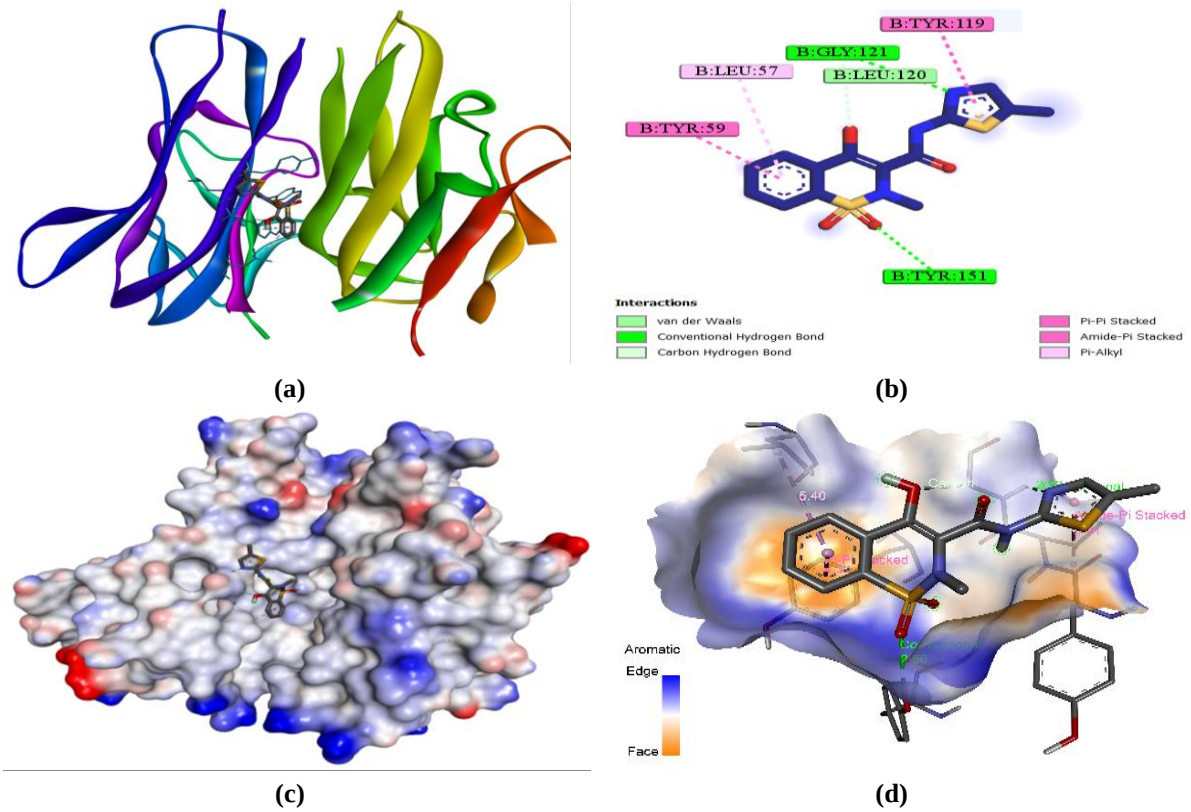

Figure 11. (a) 3D representation of TNF-α Protein(*2AZ5*)-standard drug (meloxicam) interaction; **(b)** 2D representation of TNF-α protein *2AZ5* (amino acid residue) with standard drug (meloxicam) interaction; **(c)** Interpolated charge representation of protein(*2AZ5*)- standard drug (meloxicam) complex; **(d)** Aromatic representation of protein(*2AZ5*)- standard drug (meloxicam).

3.5. MD simulation.

After compound-8b demonstrated a high binding score in molecular docking studies and met all ADMET criteria, it was selected as a lead compound and subjected to molecular dynamics simulation to assess its interactions with the TNF-α protein (*2AZ5*). This investigation revealed significant new data on the stability and dynamic characteristics of compound-8b's binding to the active regions of the TNF-α protein. This made it possible for us to assess the complex's stability and efficacy.

3.5.1. RMSD (root mean square deviation) analysis.

The Root Mean Square Deviation (RMSD) plots for the *2AZ5*-standard drug and *2AZ5*-8b complexes provide insight into the dynamic stability of the protein-ligand systems over a 100ns MD simulation. The *2AZ5*-standard drug complex exhibited moderate protein backbone (Cα) RMSD fluctuations, stabilizing around 2.5-3.0 Å after an initial equilibration phase, while the ligand RMSD remains consistently low (1.5-2.5 Å), indicating a well-retained binding conformation throughout the simulation. In contrast, the *2AZ5*-8b complex showed more pronounced fluctuations in both the protein (~5.4 Å) and ligand (~9 Å) RMSDs, suggesting greater structural deviations and potential instability of the complex. Overall, the *2AZ5*-standard drug complex exhibits a more stable RMSD profile, reflecting better conformational stability and stronger ligand retention within the binding pocket than the 2AZ5-8b complex, suggesting greater therapeutic potential.

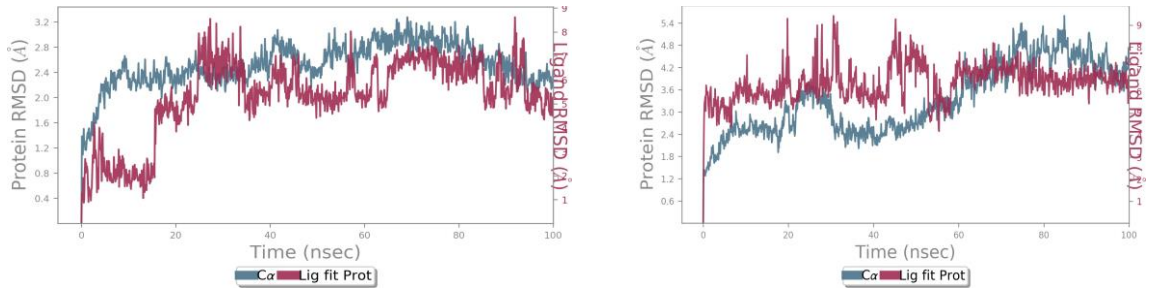

Figure 12. RMSD plot during the 100ns MD-Simulation at 300 K for **(a)** Standard drug(meloxicam)-TNF-α protein (*2AZ5*) complex; **(b)** Compound-8b- TNF-α protein (*2AZ5*) complex.

3.5.2. RMSF (root mean square fluctuation) analysis.

The Root Mean Square Fluctuation (RMSF) analysis gives information on the residue-level flexibility of the 2AZ5 protein when bound to the standard drug and the 8b compound. The RMSF profile of the 2AZ5-standard drug complex shows lower atomic fluctuations, with most residues ranging from 0.6 to 2.5 Å, indicating a more stable conformation throughout the simulation. In contrast, the 2AZ5-8b complex shows higher fluctuations, particularly at the C-terminal and loop regions, reaching up to ~4.8 Å, which suggests increased structural flexibility, which makes it advantageous in certain functional contexts, such as ligand accommodation, signaling, and drug potential, as displayed in Figure 13a and b.

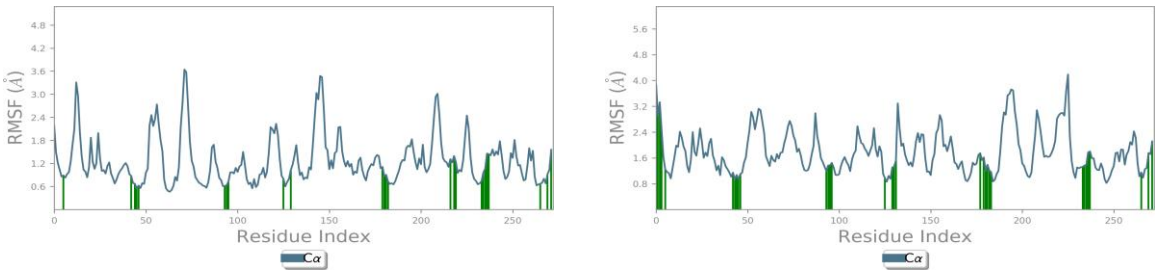

(a) **(b)**

Figure 13. RMSF plot during the 100ns MDS at 300 K for **(a)** Standard drug(meloxicam)-TNF-α protein (*2AZ5*) complex; **(b)** Compound-8b- TNF-α protein (*2AZ5*) complex.

3.5.3. Hydrogen-bond occupancy and protein-ligand interaction profiles.

The interaction profiles of 8b and the standard drug meloxicam with protein 2AZ5 revealed distinct differences in hydrogen-bond occupancy, hydrophobic interactions, and water-bridge formation. This demonstrates 8b's greater binding efficiency and stability. Hydrogen bond occupancy for 8b was significantly higher, with key protein residues such as B: SER_60 (40%), B: TYR_151 (35%), and A: TYR_119 (10%), which showed strong and stable interactions, compared to the standard drug, which showed lower occupancies of 10% with B: SER_60 and 8% with B: GLY_121. Hydrophobic interactions further strengthened the advantage of 8b, with 40% occupancy with A: TYR_59, 20% with B: VAL_123, and 20% with A: ILE_155, while meloxicam demonstrated less extensive interactions, including 55% occupancy with A: TYR_119 but weaker interactions with other residues such as B: LEU_57 (25%) and B: ILE_155 (15%).

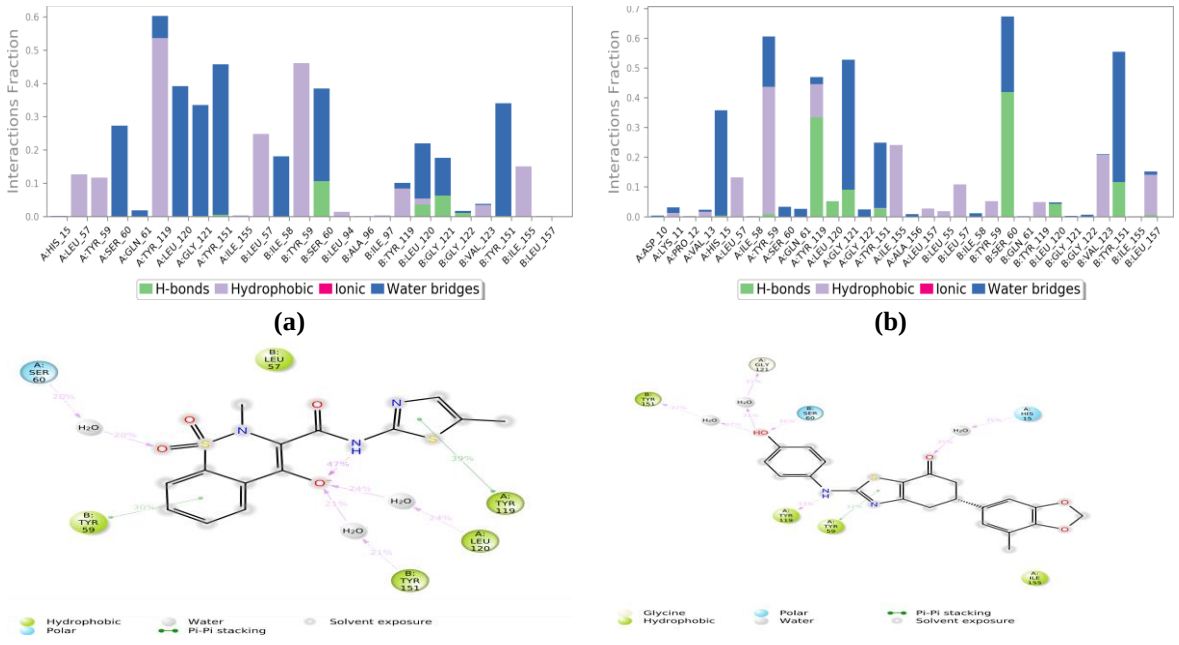

(a) **(b)**

(c) **(d)**

Figure 14. (a,b) Interactions between TNF-α protein(*2AZ5*)-standard drug (P-L Contacts) and TNF-α protein(2AZ5)-compound-8b (P-L Contacts); **(c,d)** 2D representation of protein-ligand (P-L Contacts) Interactions of TNF-α protein(*2AZ5*)-standard drug (P-L Contacts) and TNF-α protein(*2AZ5*)-compound-8b (P-L Contacts).

Furthermore, 8b formed to have more robust water bridge interactions, including 45% with B: TYR_151, 40% with A: GLY_121, and 25% with B: SER_60, compared to meloxicam, which showed fewer and weaker water bridge interactions, with a maximum of 45% with A:

TYR_151. Neither compound exhibited ionic interactions. Collectively, the stronger hydrogen bonds, broader hydrophobic interaction network, and superior water bridge formation of 8b signifies its potential as a more effective therapeutic candidate than standard drug meloxicam in stabilizing the protein-ligand complex which is demonstrated in bar graph Figure 14a and b Additionally, how the compounds (8b and standard drug) interact with specific protein (*2AZ5*) residues (amino acids) is also illustrated in Figure 14c and d.

3.6. MM-GBSA (molecular mechanics-generalized born surface area).

The MM-GBSA study is a useful method in determining the binding free energy between a compound and its target protein. Employing the MD simulation trajectory, we computed and plotted the binding free energy for 2 complexes which is demonstrated in Figure 15 The MM-GBSA analysis for the structure of the compound 8b-TNF-α protein (*2AZ5*) and Standard drug (Meloxicam)-TNF-α protein (*2AZ5*) complexes were performed by calculating the values of the binding free energy for each frame, generated over a 100 ns Molecular dynamics simulation period. Frames were collected in 10 ns increments with a step size of 100ns.

Table 5. MM-GBSA determined binding energy values for compound 8b-*2AZ5* complex and the standard drug (meloxicam-*2AZ5* complex.

MMGBSA	Compound 8b-TNF-α protein complex in kcal/mol	Standard drug - TNF-α protein complex in kcal/mol
dG_Bind	-53.6402	-36.6475
dG_Bind_Coulomb	-11.7114	-20.9585
dG_Bind_Covalent	3.5777	0.0934
dG_Bind_Hbond	-0.9431	-0.1809
dG_Bind_Lipo	-23.3406	-13.9639
dG_Bind_Packing	-1.7906	-1.9116
dG_Bind_SelfCont	0	0
dG_Bind_vdW	-37.5555	-35.4061

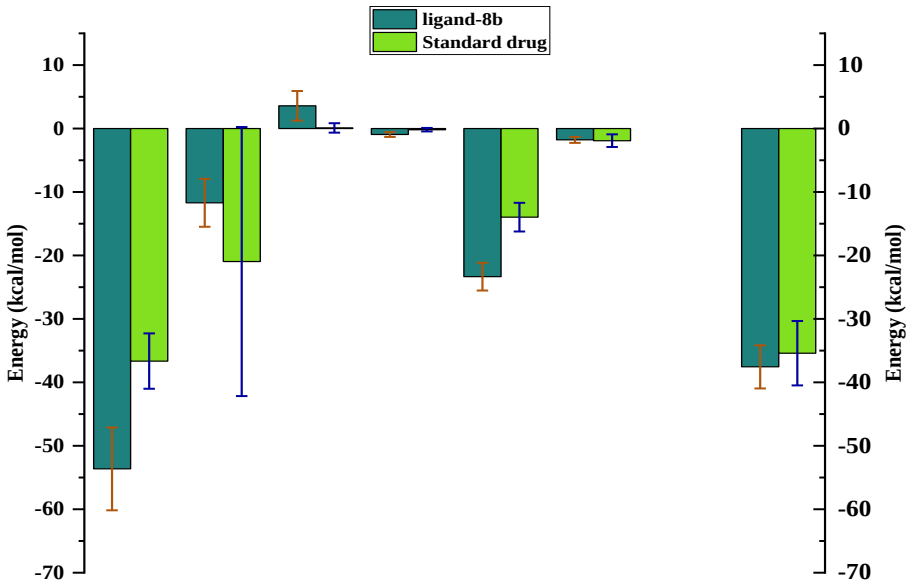

Figure 15. Calculation of Binding Energies via MM-GBSA for the TNF-α protein(*2AZ5*)-standard drug (P-L Contacts) and TNF-α protein(*2AZ5*)-compound-8b complexes.

The evaluation of the compound-8b and 2AZ5 complex revealed a high incidence of consistent negative binding free energy, with an estimated ΔGo of -53.6402 kcal/mol and a

standard deviation of ±6.5266 kcal/mol, demonstrating a significant role of net negative binding free energy in stabilizing the complex. In contrast, the Standard drug (Meloxicam) and TNF-α protein (2AZ5) complex showed higher negative binding free energy, with an estimated ΔG_o of -36.6475 kcal/mol and a standard deviation of ±4.3649 kcal/mol. This resulted in a standard drug showing a less stable and less regular binding energy than compound-8b. Along with dG_Bind and standard deviation results, other parameters such as dG_Bind_Coloumb, dG_Bind_Covalent, dG_Bind_Hbond, dG_Bind_Lipo, dG_Bind_Packing, dG_Bind_SelfCont, and dG_Bind_vdW were also calculated, in which each component helps in analyzing the contribution to binding affinity. This provides information on how the protein-ligand complexes interact and remain stable, as seen in Table 5.

4. Conclusion

A comprehensive *in silico* study, which involves pharmacophore modeling, 3D-QSAR analysis, ADMET analysis, molecular docking, and MD simulation, was performed to evaluate a lead compound as an anti-inflammatory inhibitor. Based on these results, the lead compound was found to be compound 8b, which demonstrated significant therapeutic potential as an inhibitor of the TNF-α signaling pathway (PDB ID: 2AZ5). The detailed molecular docking study revealed that 8b showed an exceptional binding score of -9.3 kcal/mol, whereas the standard anti-inflammatory drug meloxicam showed a reasonable binding score of -7.6 kcal/mol. Likewise, molecular dynamics simulations and protein-ligand interaction analysis revealed that 8b exhibits superior binding stability, interaction specificity, and occupancy in comparison to the standard drug meloxicam. Furthermore, it established more significant water bridges, hydrophobic contacts, and hydrogen bonds with key protein residues, suggesting enhanced binding efficiency and stability. Moreover, its higher occupancy percentages across key protein residues also highlighted its robustness as a therapeutic candidate. All these results highlighted compound-8b's effectiveness as a promising anti-inflammatory agent, with potential applications in targeting TNF-α-mediated chronic conditions. However, the lack of experimental validation, such as in vitro and in vivo studies, limits the applicability of these *in silico* results.

Supplementary materials

Download here

Author Contributions

Conceptualization – S.N.; Methodology – S.N.; Validation – S.N.; Investigation – S.N.; Formal analysis – M.P.; Software – M.P., D.P.P.; Writing – original draft preparation – M.P., D.P.P.; Writing – review & editing – S.A.S., S.S., P.M.; Supervision – S.N., S.A.S., S.S. All authors have read and agreed to the published version of the manuscript.

Institutional Review Board Statement

Not applicable.

Informed Consent Statement

Not applicable.

Data Availability Statement

All the data and supporting information are provided in the article and the supplementary file.

Funding

This research received no external funding.

Acknowledgement

The authors are thankful to JSS Science and Technology University, Mysuru 570 006, India, for providing necessary support and facilities.

Conflicts of Interest

The authors declare no conflict of interest.

References

1. Arshad, M.F.; Alam, A.; Alshammari, A.A.; Alhazza, M.B.; Alzimam, I.M.; Alam, M.A.; Mustafa, G.; Ansari, M.S.; Alotaibi, A.M.; Alotaibi, A.A.; Kumar, S. Thiazole: A Versatile Standalone Moiety Contributing to the Development of Various Drugs and Biologically Active Agents. *Molecules* **2022**, *27*, 3994, https://doi.org/10.3390/molecules27133994.
2. Hosseininezhad, S.; Ramazani, A. Thiazole Ring—The Antimicrobial, Anti-Inflammatory, and Anticancer Active Scaffold. *Arab. J. Chem.* **2023**, *16*, 105234, https://doi.org/10.1016/j.arabjc.2023.105234.
3. Borcea, A.M.; Ionuț, I.; Crișan, O.; Oniga, O. An Overview of the Synthesis and Antimicrobial, Antiprotozoal, and Antitumor Activity of Thiazole and Bisthiazole Derivatives. *Molecules* **2021**, *26*, 624, https://doi.org/10.3390/molecules26030624.
4. Ebaid, M.S.; Ibrahim, H.A.; Kassem, A.F.; Sabt, A. Recent Studies on Protein Kinase Signaling Inhibitors Based on Thiazoles: Review to Date. *RSC Adv.* **2024**, *14*, 36989–37018, https://doi.org/10.1039/D4RA05601A.
5. Mishra, R.; Sharma, P.K.; Verma, P.K.; Tomer, I.; Mathur, G.; Dhakad, P.K. Biological Potential of Thiazole Derivatives of Synthetic Origin. *J. Heterocycl. Chem.* **2017**, *54*, 2103–2116, https://doi.org/10.1002/jhet.2914.
6. Tarı Selçuk, K. Epidemiology of Inflammation-Related Diseases. In Role of Nutrition in Providing Pro-/Anti-Inflammatory Balance: Emerging Research and Opportunities, Günşen, U., Atan, R.M., Eds.; IGI Global Scientific Publishing: Hershey, PA, USA, **2020**; pp. 24-44, https://doi.org/10.4018/978-1-7998-3594-3.ch002.
7. Jairath, V.; Feagan, B.G. Global Burden of Inflammatory Bowel Disease. *Lancet Gastroenterol. Hepatol.* **2020**, *5*, 2–3, https://doi.org/10.1016/s2468-1253(19)30358-9.
8. Nowarski, R.; Gagliani, N.; Huber, S.; Flavell, R.A. Innate Immune Cells in Inflammation and Cancer. *Cancer Immunol. Res.* **2013**, *1*, 77–84, https://doi.org/10.1158/2326-6066.CIR-13-0077.
9. Fioranelli, M.; Roccia, M.G.; Flavin, D.; Cota, L. Regulation of Inflammatory Reaction in Health and Disease. *Int. J. Mol. Sci.* **2021**, *22*, 5277, https://doi.org/10.3390/ijms22105277.
10. Wajant, H.; Siegmund, D. TNFR1 and TNFR2 in the Control of the Life and Death Balance of Macrophages. *Front. Cell Dev. Biol.* **2019**, *7*, 91, https://doi.org/10.3389/fcell.2019.00091.
11. Solitano, V.; Yuan, Y.; Singh, S.; Ma, C.; Nardone, O.M.; Fiorino, G.; Felquer, M.L.; Barra, L.; D'Agostino, M.A.; Pope, J.; Peyrin-Biroulet, L. Efficacy and Safety of Advanced Combination Treatment in Immune-Mediated Inflammatory Disease: A Systematic Review and Meta-Analysis of Randomized Controlled Trials. *J. Autoimmun.* **2024**, *149*, 103331, https://doi.org/10.1016/j.jaut.2024.103331.
12. Zhao, H.; Wu, L.; Yan, G.; Chen, Y.; Zhou, M.; Wu, Y.; Li, Y. Inflammation and Tumor Progression: Signaling Pathways and Targeted Intervention. *Signal Transduct. Target. Ther.* **2021**, *6*, 263, https://doi.org/10.1038/s41392-021-00658-5.

13. Kong, D.H.; Kim, Y.K.; Kim, M.R.; Jang, J.H.; Lee, S. Emerging Roles of Vascular Cell Adhesion Molecule-1 (VCAM-1) in Immunological Disorders and Cancer. *Int. J. Mol. Sci.* **2018**, *19*, 1057, https://doi.org/10.3390/ijms19041057.
14. Shin, J.Y.; Park, J.H.; Cho, B.O.; Kang, E.S.; Joo, M.H.; Kim, Y.S.; Jang, S.I. Protective Effects of Angelica keiskei Extract against TNF-α-Induced Oxidative Stress and Vascular Inflammation in Human Umbilical Vein Endothelial Cells. *Food Sci. Preserv.* **2024**, *31*, 590–600, https://doi.org/10.11002/fsp.2024.31.4.590.
15. Jang, D.I.; Lee, A.H.; Shin, H.Y.; Song, H.R.; Park, J.H.; Kang, T.B.; Yang, S.H. The Role of Tumor Necrosis Factor Alpha (TNF-α) in Autoimmune Disease and Current TNF-α Inhibitors in Therapeutics. *Int. J. Mol. Sci.* **2021**, *22*, 2719, https://doi.org/10.3390/ijms22052719.
16. Tamatam, R.; Shin, D. Asymmetric Synthesis of US-FDA Approved Drugs over Five Years (2016–2020): A Recapitulation of Chirality. *Pharmaceuticals* **2023**, *16*, 339, https://doi.org/10.3390/ph16030339.
17. Chalkha, M.; Akhazzane, M.; Moussaid, F.Z.; Daoui, O.; Nakkabi, A.; Bakhouch, M.; El Yazidi, M. Design, Synthesis, Characterization, In Vitro Screening, Molecular Docking, 3D-QSAR, and ADME-Tox Investigations of Novel Pyrazole Derivatives as Antimicrobial Agents. *New J. Chem.* **2022**, *46*, 2747–2760, https://doi.org/10.1039/D1NJ05621B.
18. Philips, A.; Arumugam, A.; Eswaramoorthy, Y.; Boominathan, S.S.K.; Senadi, G.C. Iodine-Mediated Three-Component Strategy to Synthesize 2-Aminothiazoles from β-Diketones/β-Ketoesters, Arylamines and Ammonium Thiocyanate. *Eur. J. Org. Chem.* **2022**, *46*, e202201233, https://doi.org/10.1002/ejoc.202201233.
19. Alanzi, A.R.; Moussa, A.Y.; Alsalhi, M.S.; Nawaz, T.; Ali, I. Integration of Pharmacophore-Based Virtual Screening, Molecular Docking, ADMET Analysis, and MD Simulation for Targeting EGFR: A Comprehensive Drug Discovery Study Using Commercial Databases. *PLoS ONE* **2024**, *19*, e0311527, https://doi.org/10.1371/journal.pone.0311527.
20. Qandeel, B.M.; Mowafy, S.; Abouzid, K.; Farag, N.A. Lead Generation of UPPS Inhibitors Targeting MRSA: Using 3D-QSAR Pharmacophore Modeling, Virtual Screening, Molecular Docking, and Molecular Dynamic Simulations. *BMC Chem.* **2024**, *18*, 14, https://doi.org/10.1186/s13065-023-01110-1.
21. Filimonov, D.A.; Lagunin, A.A.; Gloriozova, T.A.; Rudik, A.V.; Druzhilovskii, D.S.; Pogodin, P.V.; Poroikov, V.V. Prediction of the Biological Activity Spectra of Organic Compounds Using the PASS Online Web Resource. *Chem. Heterocycl. Compd.* **2014**, *50*, 444–457, https://doi.org/10.1007/s10593-014-1496-1.
22. Sheng, S.; Yang, Z.X.; Xu, F.Q.; Huang, Y. Network Pharmacology-Based Exploration of Synergistic Mechanism of Guanxin II Formula for Coronary Heart Disease. *Chin. J. Integr. Med.* **2020**, *27*, 106-114, https://doi.org/10.1007/s11655-020-3199-z.
23. Wu, L.; Wang, Q.; Gao, Q.C.; Shi, G.X.; Li, J.; Fan, F.R.; Wu, J.; He, P.F.; Yu, Q. Potential Mechanisms and Drug Prediction of Rheumatoid Arthritis and Primary Sjögren's Syndrome: A Public Databases-Based Study. *PLoS ONE* **2024**, *19*, e0298447, https://doi.org/10.1371/journal.pone.0298447.
24. Tamer, F.; Edek, Y.C.; Aksakal, A.B. Effect of Treatment with Biologic Agents on the Novel Inflammatory Biomarkers Systemic Immune Inflammation Index and Systemic Inflammation Response Index for Psoriasis. *Dermatol. Pract. Concept.* **2024**, *14*, e2024065, https://doi.org/10.5826/dpc.1401a65.
25. UniProt Consortium. UniProt: A Hub for Protein Information. *Nucleic Acids Res.* **2015**, *43*, D204–D212, https://doi.org/10.1093/nar/gku989.
26. Bai, L.L.; Chen, H.; Zhou, P.; Yu, J. Identification of Tumor Necrosis Factor-Alpha (TNF-α) Inhibitor in Rheumatoid Arthritis Using Network Pharmacology and Molecular Docking. *Front. Pharmacol.* **2021**, *12*, 690118, https://doi.org/10.3389/fphar.2021.690118.
27. Szklarczyk, D.; Gable, A.L.; Lyon, D.; Junge, A.; Wyder, S.; Huerta-Cepas, J.; von Mering, C. STRING v11: Protein–Protein Association Networks with Increased Coverage, Supporting Functional Discovery in Genome-Wide Experimental Datasets. *Nucleic Acids Res.* **2019**, *47*, D607–D613, https://doi.org/10.1093/nar/gky1131.
28. Ma, G.; Dong, Q.; Li, F.; Jin, Z.; Pi, J.; Wu, W.; Li, J. Network Pharmacology and In Vivo Evidence of the Pharmacological Mechanism of Geniposide in the Treatment of Atherosclerosis. *BMC Complement. Med. Ther.* **2024**, *24*, 53, https://doi.org/10.1186/s12906-024-04356-x.
29. Jin, J.; Chen, B.; Zhan, X.; Zhou, Z.; Liu, H.; Dong, Y. Network Pharmacology and Molecular Docking Study on the Mechanism of Colorectal Cancer Treatment Using Xiao-Chai-Hu-Tang. *PLoS ONE* **2021**, *16*, e0252508, https://doi.org/10.1371/journal.pone.0252508.

30. Ding, K.; Gulec, A.; Johnson, A.M.; Schweitzer, N.M.; Stucky, G.D.; Marks, L.D.; Stair, P.C. Identification of Active Sites in CO Oxidation and Water-Gas Shift over Supported Pt Catalysts. *Science* **2015**, *350*, 189–192, https://doi.org/10.1126/science.aac6368.
31. de Sousa, N.F.; de Araújo, I.M.; Moreira Lustoza Rodrigues, T.C.; da Silva, P.R.; de Moura, J.P.; Scotti, M.T.; Scotti, L. Proposition of *In silico* Pharmacophore Models for Malaria: A Review. *Comb. Chem. High Throughput Screen.* **2024**, *27*, 2525–2543, https://doi.org/10.2174/0113862073247691230925062440.
32. Rohini, K.; Ramanathan, K.; Shanthi, V. Multi-Dimensional Screening Strategy for Drug Repurposing with Statistical Framework—A New Road to Influenza Drug Discovery. *Cell Biochem. Biophys.* **2019**, *77*, 319–333, https://doi.org/10.1007/s12013-019-00887-0.
33. James, J.P.; Devaraji, V.; Sasidharan, P.; TS, P. Pharmacophore Modeling, 3D QSAR, Molecular Dynamics Studies and Virtual Screening on Pyrazolopyrimidines as Anti-Breast Cancer Agents. *Polycycl. Aromat. Compd.* **2022**, 43, 7456-7473, https://doi.org/10.1080/10406638.2022.2135545.
34. Sharma, S.; Basu, A.; Agrawal, R.K. Pharmacophore Modeling and Docking Studies on Some Nonpeptide-Based Caspase-3 Inhibitors. *Biomed Res. Int.* **2013**, *2013*, 306081, https://doi.org/10.1155/2013/306081.
35. Bebia, G.P.; Edet, U.O.; Eyo, A.A.O.; Ugwu, J.C.; Mbim, E.N.; Ogba, O.M.; Nwaokorie, F.O. Evaluation of Bioactive Compounds in *Tetrapleura tetraptera* (Uyayak) and Its Activity Against Dihydropteroate Synthase (1AJ2) of *E. coli*: Insight from ADMET Profiling and Molecular Docking. *Nat. Prod. Commun.* **2024**, *19*, 1934578X241284045, https://doi.org/10.1177/1934578X241284045.
36. Nanjundaswamy, S.; Hema, M.K.; Karthik, C.S.; Rajabathar, J.R.; Arokiyaraj, S.; Lokanath, N.K.; Mallu, P. Synthesis, Crystal Structure, In-Silico ADMET, Molecular Docking and Dynamics Simulation Studies of Thiophene-Chalcone Analogues. *J. Mol. Struct.* **2022**, *1247*, 131365, https://doi.org/10.1016/j.molstruc.2021.131365.
37. Abd El-Karim, S.S.; Mohamed, H.S.; Abdelhameed, M.F.; Amr, A.E.G.E.; Almehizia, A.A.; Nossier, E.S. Design, Synthesis and Molecular Docking of New Pyrazole-Thiazolidinones as Potent Anti-Inflammatory and Analgesic Agents with TNF-α Inhibitory Activity. *Bioorg. Chem.* **2021**, *111*, 104827, https://doi.org/10.1016/j.bioorg.2021.104827.
38. Afriza, D.; Orienty, F.N.; Ayu, W.P. Molecular Docking Analysis of the Interactions Between MMP-9 Protein and Four Coumarin Compounds (Nordentatin, Dentatin, Calusenidin and Xanthoxyletin). *J. Int. Dent. Med. Res.* **2020**, *13*, 1286–1292.
39. Rasul, H.O.; Aziz, B.K.; Ghafour, D.D.; Kivrak, A. *In silico* Molecular Docking and Dynamic Simulation of Eugenol Compounds Against Breast Cancer. *J. Mol. Model.* **2022**, *28*, 17, https://doi.org/10.1007/s00894-021-05010-w.
40. Broni, E.; Striegel, A.; Ashley, C.; Sakyi, P.O.; Peracha, S.; Velazquez, M.; Miller, W.A. III. Molecular Docking and Dynamics Simulation Studies Predict Potential Anti-ADAR2 Inhibitors: Implications for the Treatment of Cancer, Neurological, Immunological and Infectious Diseases. *Int. J. Mol. Sci.* **2023**, *24*, 6795, https://doi.org/10.3390/ijms24076795.
41. Hema, M.K.; ArunRenganathan, R.R.; Nanjundaswamy, S.; Karthik, C.S.; Mohammed, Y.H.I.; Alghamdi, S.; Mallu, P. *N*-(4-Bromobenzylidene)-2,3-Dihydrobenzo[b][1,4]Dioxin-6-Amine: Synthesis, Crystal Structure, Docking and In-Vitro Inhibition of PLA2. *J. Mol. Struct.* **2020**, *1218*, 128441, https://doi.org/10.1016/j.molstruc.2020.128441.
42. Nanjundaswamy, S.; Bindhu, S.; Arun Renganathan, R.R.; Nagashree, S.; Karthik, C.S.; Mallu, P.; Ravishankar Rai, V. Design, Synthesis of Pyridine Coupled Pyrimidinone/Pyrimidinthione as Anti-MRSA Agent: Validation by Molecular Docking and Dynamics Simulation. *J. Biomol. Struct. Dyn.* **2022**, *40*, 12106–12117, https://doi.org/10.1080/07391102.2021.1968496.
43. Ahmad, S.; Bhanu, P.; Kumar, J.; Pathak, R.K.; Mallick, D.; Uttarkar, A.; Mishra, V. Molecular Dynamics Simulation and Docking Studies Reveal NF-κB as a Promising Therapeutic Drug Target for COVID-19. *Preprints* **2021**, https://doi.org/10.21203/rs.3.rs-469785/v2.
44. Swamy, P.M.; Somashekar, P.H.; Shivamurthy, S.A.; Shadakshari, S.; Puttaswamappa, M.; Shanthappa, N.S. Design, synthesis, and in silico evaluation of 2-aminothiazole derivatives as potential mTOR and EGFR inhibitors. *Discover Molecules* **2025**, 2, 31, https://doi.org/10.1007/s44345-025-00039-3.
45. Choudhary, M.I.; Shaikh, M.; tul-Wahab, A.; ur-Rahman, A. *In silico* Identification of Potential Inhibitors of Key SARS-CoV-2 3CL Hydrolase (Mpro) via Molecular Docking, MMGBSA Predictive Binding Energy Calculations, and Molecular Dynamics Simulation. *PLoS ONE* **2020**, 15, e0235030, https://doi.org/10.1371/journal.pone.0235030.

46. Yang, X.; Huang, Y.; Tang, D.; Yue, L. Identification of Key Genes Associated with Acute Myocardial Infarction Using WGCNA and Two-Sample Mendelian Randomization Study. *PLoS ONE* **2024**, *19*, e0305532, https://doi.org/10.1371/journal.pone.0305532.
47. Yan, F.; Liu, Y.; Zhang, T.; Shen, Y. Identifying TNF and IL6 as Potential Hub Genes and Targeted Drugs Associated with Scleritis: A Bio-Informative Report. *Front. Immunol.* **2023**, *14*, 1098140, https://doi.org/10.3389/fimmu.2023.1098140.
48. Kalliolias, G.D.; Ivashkiv, L.B. TNF Biology, Pathogenic Mechanisms and Emerging Therapeutic Strategies. *Nat. Rev. Rheumatol.* **2016**, *12*, 49–62, https://doi.org/10.1038/nrrheum.2015.169.
49. Lis, K.; Kuzawińska, O.; Bałkowiec-Iskra, E. Tumor Necrosis Factor Inhibitors—State of Knowledge. *Arch. Med. Sci.* **2014**, *10*, 1175–1185, https://doi.org/10.5114/aoms.2014.47827.
50. Oală, I.E.; Mitranovici, M.I.; Chiorean, D.M.; Irimia, T.; Crișan, A.I.; Melinte, I.M.; Pușcașiu, L. Endometriosis and the Role of Pro-Inflammatory and Anti-Inflammatory Cytokines in Pathophysiology: A Narrative Review of the Literature. *Diagnostics* **2024**, *14*, 312, https://doi.org/10.3390/diagnostics14030312.
51. Zheng, Z.; Lei, J.; Chang, J.; Yi, X.; Zhou, G.; Chen, J. Exploring the Mechanisms of the Huangqin Qingfei Decoction in Pneumonia Treatment for Lipopolysaccharide-Induced Mouse Model: A Network Pharmacology Analysis and Experimental Validation. *Nat. Prod. Commun.* **2024**, *19*, 1934578X241239843, https://doi.org/10.1177/1934578X241239843.
52. Mishra, N.; Maurya, A.K. Novel Drug Discovery Against Breast and Lung Cancer Using Pharmacophore Based 2H-1-Benzopyran-2-One Derivative. *Preprints* **2022**, https://doi.org/10.21203/rs.3.rs-1541154/v1.

Publisher's Note & Disclaimer